Improved Analytical Modeling of a Novel Ironless Linear Synchronous Machine With Asymmetrical Double-Layer Winding Topology

Zhedong Xie, Qinfen Lu, *Senior Member, IEEE*, Weihu Mei, and Yanxin Li

***Abstract*—The Ironless Permanent Magnet Linear Synchronous Motor (ILPMLSM) with nonoverlapping windings is widely used in precise applications due to its simple structure, low thrust ripple, and fast response, while the disadvantage is low thrust density. The novel asymmetrical double-layer winding ILPMLSM with quasi-Halbach magnets can improve the thrust density while keeping simple structure. However, the double-layer windings are asymmetric and the primary has finite length. To solve the problem of this asymmetry and investigate its influences on electromagnetic characteristics, an improved 2-D analytical model is proposed, which introduces "virtual periodic primary" and solves the magnetic field of each winding layer. By the results of finite element and experiments, the proposed analytical model is verified. Moreover, the analytical model requires less computation time, which is helpful for optimizing design of this motor.**

***Index Terms*—Analytical model, asymmetry, double-layer windings, ironless permanent magnet linear synchronous motor (ILPMLSM), longitudinal end effect.**

I. Introduction

THE Ironless Permanent Magnet Linear Synchronous Motor (ILPMLSM) is characterized by low thrust ripple, fast response and easy control. Therefore, it is widely used in precision applications such as semiconductor processing device, *X–Y* driving devices, automation equipment, etc., [1]–[3]. However, the thrust density of ILPMLSM is low due to the ironless structure. To further increase the thrust density, some existing research has tried to adjust the magnetic poles, for instance using quasi-Halbach arrays [4]. Besides, the layout of windings can be changed since the ironless structure provides more freedom without slot constraints. The three-layer and double-layer winding configurations are introduced [5]–[7], and the comparative study has been made with the traditional single-layer structures [6], [7]. Placing three-phase winding into two layers can increase winding factor, while the space utilization issue and processing difficulty caused by the overlapping ends of single-layer distributed winding can be eliminated [6]. Although the adoption of double-layer winding configuration can enlarge the thrust density, it will cause winding asymmetry. The influence of this asymmetry on electromagnetic performance has not been discussed in [6] analytically.

As it is common to apply ILPMLSM in high-demanding applications, accurate modeling is an essential part in the design, optimization and control of motors. Finite-element analysis (FEA) can be rather time consuming while analytical model can accurately describe all complicated boundaries and save much time. However, none of [6] and [7] builds up an analytical model considering the asymmetry. An overview of analytical techniques for linear and planar motor concludes that the surface charge models are essential for the planar motor and coreless linear motor, while harmonic model is the most suitable method for 2-D analysis of slotless motors [8]. Surface charge models can describe the field of separate PMs and can be applied to structures without slotting [9]. As for harmonic model, many analytical models of linear motors have been proposed in previously published work [10]–[18]. The calculations of no-load PM field for various magnetization patterns have been widely studied [10]–[14], especially for quasi-Halbach arrays [13], [14]. And the longitudinal end effect of linear motor is considered by adding virtual slots to the subdomain model [15]. Armature reaction field is calculated mainly to deduce the inductances required for high-precision motion control. However, finite length of the primary/secondary (or longitudinal end effect) is rarely considered in previous work. Neglecting the longitudinal end effect may introduce a direct current-bias (dc-bias) of air-gap flux density [16], which will reduce the precision of the analytical model. Hence, subdomain model considering the end regions is proposed, and the magnetic field is calculated in [16] and [17]. It is complicated to include additional sub-regions, however. Thus, equivalent magnetic circuit method considering the finite length of motor is applied to compute the armature reaction field precisely [18]. To model more complex structures, a Hybrid Analytical Model (HAM) is introduced, combining the advantages of analytical solution of Maxwell's equations and

Manuscript received June 26, 2020; revised November 15, 2020; accepted December 22, 2020. Date of publication December 30, 2020; date of current version March 17, 2021. Paper 2020-EMC-0952.R1, presented at the 22nd International Conference on Electrical Machines and Systems, Harbin, China, Aug. 11–14, and approved for publication in the IEEE Transactions on Industry Applications by the Electric Machines Committee of the IEEE Industry Applications Society. This work was supported in part by the Zhejiang Provincial Natural Science Foundation of China under Grant LZ17E070001 and in part by the Ningbo Science and Technology Innovation 2025 major project under Grant 2018B10068. *(Corresponding author: Qinfen Lu.)*

Zhedong Xie, Weihu Mei, and Yanxin Li are with the College of Electrical Engineering, Zhejiang University, Hangzhou 310027, China, (e-mail: 21810058@zju.edu.cn; 3120102352@zju.edu.cn; eeliyanxin@zju.edu.cn).

Qinfen Lu was with the College of Electrical Engineering, Zhejiang University, Hangzhou 310027, China, and also with the Lanzhou University of Technology, Lanzhou 730000, China (e-mail: luqinfen@zju.edu.cn).

Color versions of one or more of the figures in this article are available online at https://doi.org/10.1109/TIA.2020.3048325.

Digital Object Identifier 10.1109/TIA.2020.3048325

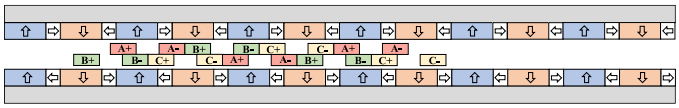

Fig. 1. Schematic of a 9s/6p DW-ILPMLSM with quasi-Halbach magnets.

reluctance networks [19]. Furthermore, HAM in [20] combines the equivalent magnetic circuit and Finite Element (FE) method for air-cored linear motor.

To investigate the influence of winding asymmetry and longitudinal ends on electromagnetic performance, a 9-slot/6-pole (9s/6p) Double-layer Winding-ILPMLSM (DW-ILPMLSM) with quasi-Halbach magnets is studied in this article. FEA is mainly used to investigate the performance of DW-ILPMLSM in [7]. However, a comprehensive accurate analytical model considering the winding asymmetry and the finite length of moving primary is proposed in this article. It not only helps to understand the influence of motor parameters on performance, but also helps to optimize the motor structure faster. FEA and experimental tests are conducted to prove the feasibility of the proposed analytical model. For some rotary fractional-slot motors, the asymmetric windings will lead to Unbalanced Magnetic Force (UMF), which causes vibration and noise [21], [22]. For bilateral linear motors with asymmetric windings, the normal force is similar with UMF which is caused by the asymmetry. Obviously, the thrust will also be affected by this asymmetry. Thus, the force performance, including normal force, average thrust and thrust ripple are mainly studied in this article.

The rest of this article is organized as follows: In Section II, the proposed 9s/6p DW-ILPMLSM model is introduced. DW-ILPMLSM is analyzed using both analytical and FE model in Section III. Then, the force performance is investigated, and the winding asymmetrical property of the DW-ILPMLSM is fully discussed in Section IV. The experiments are conduct in Section V. Finally, the corresponding conclusion is drawn in Section VI.

II. Motor Structure

Fig. 1 shows the 2-D topology of a 9s/6p DM-ILPMLSM. It has short primary and long secondary. Its moving primary consists of air-core double-layer concentrated winding. The upper layer consists of four coils while the lower layer consists of five coils. All of the coils are molded by epoxy resin. Besides, the three-phase winding is star-connected. The secondary consists of two quasi-Halbach Permanent Magnet (PM) arrays and back-irons, forming a bilateral structure. This DM-ILPMLSM is developed based on a normal ILPMLSM, therefore several parameters are fixed, including velocity, frequency, and electromagnetic force. Therefore, the double layer windings are main design objective.

In order to obtain the maximum thrust density under the fixed outer volume and copper loss, several key parameters are optimized by FEA. Constraints are also kept during the optimization process, including the reasonable range of the pole pitch, turns per phase, etc. The aim of optimization was to increase the average-thrust-to-thrust-ripple ratio. The detailed

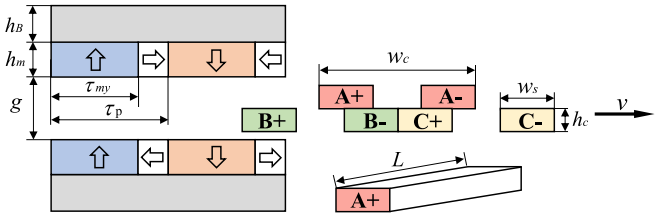

Fig. 2. Geometric parameters of the DW-ILPMLSM.

TABLE I
Main Design Parameters

Symbol	Parameter	Value
τ_p	Pole pitch	20.2 mm
τ_c	Coil pitch	13.47 mm
h_B	Back iron thickness	6.3 mm
h_m	Magnet thickness	6.0 mm
τ_{my}	Main Magnet width	15.0 mm
g	Air-gap length	9.6 mm
w_s	Coil width	9.3 mm
h_c	Coil thickness	4.0 mm
w_c	Coil span	26.93 mm
L	Active length along z-axis	60 mm
v	Velocity of the mover	2.02 m/s
N_s	Turns per coil	48
W_m	Overall machine width	34.2 mm
L_m	Overall machine length	296.8 mm

dimensions and specifications are shown in Fig. 2 and Table I. As adjacent coils are in close contact from Fig. 1, the coil span $w_c = 2\,\tau_c = 4\tau_p/3$.

III. Analytical Modeling

Subdomain method is adopted in this article to analyze the magnetic field. Because the air-gap is large enough, the ILPMLSM is hardly saturated. The FE result under full-load condition that the maximum flux density in the secondary yoke is about 1.7 T also confirms it. Thus, the resultant magnetic field can be obtained by the superposition of no-load PM field and armature reaction field [23].

To simplify 2-D analysis, assumptions are made as follows:

1) the permeability of back-irons is infinite and the permeability of PMs is equal to that of air;
2) PMs are periodically distributed in x-axis;
3) the transverse end effect is ignored; and
4) all regions extend infinitely in x-axis.

A. No-Load PM Field

In the x–y coordinate system, the analytical model of the no-load PM field is divided into three sub-regions shown in Fig. 3: air-gap region I, PM region II and back-iron region III.

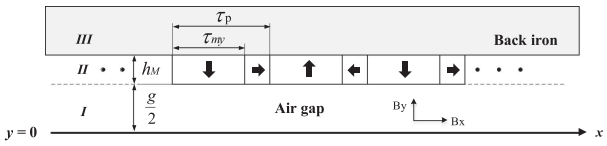

Fig. 3. Analytical model of no-load PM field.

Based on Maxwell equations, the governing equation of each region is given as

$$\nabla^2 \overrightarrow{A_{I,\,III}} = 0$$
$$\nabla^2 \vec{A}_{II} = -\mu_0 \nabla \times \vec{M} \tag{1}$$

where A is the magnetic vector potential; μ_0 is the permeability of free space and M is the remanent magnetic intensity. Using equivalent magnetizing current method [2]–[23], equivalent surface current density of quasi-Halbach arrays can be expressed by the curl of magnetic intensity M shown in (1). The quasi-Halbach arrays have PMs excited in x- and y-directions, whose magnetic intensity M is given by

$$\vec{M} = M_x \overrightarrow{e_x} + M_y \overrightarrow{e_y} \tag{2}$$

where M_x and M_y are the x and y components of magnetic intensity M, respectively. Although linear motors have end effect, the length of secondary is long enough relative to that of primary, which means assumption (2) will introduce little error in analyzing the no-load PM field. So the magnetic intensity can be expressed by Fourier series as follows:

$$\begin{cases} M_x = \sum\limits_{n=1}^{\infty} \frac{4B_r}{m_n \tau_p \mu_0} \cos\left(\frac{m_n \tau_{my}}{2}\right) \sin\left(m_n x\right) \\ M_y = \sum\limits_{n=1}^{\infty} \frac{4B_r}{m_n \tau_p \mu_0} \sin\left(\frac{m_n \tau_{my}}{2}\right) \cos\left(m_n x\right) \end{cases} \tag{3}$$

where B_r is the remanence of PM, τ_p is the pole pitch, τ_{my} is the width of PMs magnetized in y direction, m_n is given by

$$m_n = (2n-1)\frac{\pi}{\tau_p}. \tag{4}$$

By applying the variable separation method, the general solutions of Laplace/Poisson equation can be obtained

$$\begin{cases} A_{zI} = \sum\limits_{n=1}^{\infty} \left[A_{nI} \sin h\left(m_n y\right) + B_{nI} \cos h\left(m_n y\right)\right] \sin\left(m_n x\right) \\ A_{zII} = \sum\limits_{n=1}^{\infty} \left[A_{nII} \sin h\left(m_n y\right) + B_{nII} \cos h\left(m_n y\right) + P_n\right] \\ \qquad \sin\left(m_n x\right) \end{cases} \tag{5}$$

where the particular solution P_n is given by

$$P_n = -\frac{4B_r \sin\left(\frac{m_n \tau_{my}}{2}\right)}{m_n^2 \tau_p} \tag{6}$$

All of the coefficients A_{nI}, A_{nII}, B_{nI}, and B_{nII} can be deduced from the following boundary conditions:

$$\begin{cases} B_{yI}\,|_{y=\frac{g}{2}} = B_{yII}\,|_{y=\frac{g}{2}} \;;\; H_{xII}|_{y=\frac{g}{2}} - H_{xI}\,|_{y=\frac{g}{2}} = M_x \\ H_{xII}\,|_{y=\frac{g}{2}+h_m} = M_x \;;\; H_{xI}\,|_{y=0} = 0 \end{cases}. \tag{7}$$

TABLE II
BACK-EMF HARMONICS

Harmonic order		E_A (V)	E_B (V)	E_C (V)
1st (50Hz)	Analytical	26.91	26.91	26.91
	FE	26.27	26.27	26.27
3rd (150Hz)	Analytical	1.38	1.38	1.38
	FE	1.34	1.34	1.34
5th (250Hz)	Analytical	0.03	0.03	0.03
	FE	0.03	0.01	0.04

The tangential direction is denoted by subscript "x" and the normal direction is denoted by subscript "y." So, the tangential and normal components of air-gap flux density are deduced by magnetic vector potential A_{zI} as follows:

$$\begin{cases} B_{yI} = -\sum\limits_{n=1}^{\infty} m_n \left[A_{nI} \sin h\left(m_n y\right) + B_{nI} \cos h\left(m_n y\right)\right] \\ \qquad \cos\left(m_n x\right) \\ B_{xI} = \sum\limits_{n=1}^{\infty} m_n \left[A_{nI} \cos h\left(m_n y\right) + B_{nI} \sin h\left(m_n y\right)\right] \\ \qquad \sin\left(m_n x\right). \end{cases} \tag{8}$$

The no-load flux density of air-gap enables the prediction of the back electromotive force (back-EMF). Accounting for the displacement of the moving primary $x_0 = vt$, the back-EMF of phase A is given by

$$E_A = E_{A_+} - E_{A_-} = N_c \int_0^{h_c} \int_{-\frac{w_c}{2}+x_0}^{-\frac{w_c}{2}+w_s+x_0} \frac{N_s}{h_c w_s} B_{yI} L v dx dy - N_c \int_0^{h_c} \int_{\frac{w_c}{2}-w_s+x_0}^{\frac{w_c}{2}+x_0} \frac{N_s}{h_c w_s} B_{yI} L v dx dy \tag{9}$$

E_A is finally simplified as

$$E_A = \sum_{n=1}^{\infty} A_E \sin h\left(m_n h_c\right) \cdot \sin\left(m_n v t\right). \tag{10}$$

The coefficient A_E is given by

$$A_E = -\frac{2N_c N_s L v B_{nI}}{h_C w_s m_n} \left\{\cos\left[m_n\left(\frac{w_C}{2} - w_s\right)\right] - \cos\left(\frac{m_n w_C}{2}\right)\right\} \tag{11}$$

where N_c is the number of coils per phase and N_s is the number of turns per coil. The amplitudes of the main harmonics of back-EMF are given in Table II using (10) and (11). Because the windings are star-connected, the third harmonic will be cancelled. Besides, the amplitude of fifth harmonic is 0.1% of the fundamental. So the harmonics of back-EMF can be neglected.

B. Armature Reaction Field

When analyzing the armature reaction field of a DW-ILPMLSM, the longitudinal end effect and asymmetry of double-layer windings should be considered to obtain an accurate result.

First, attention should be paid that the assumptions (4) will introduce a dc-bias of armature reaction field because of the

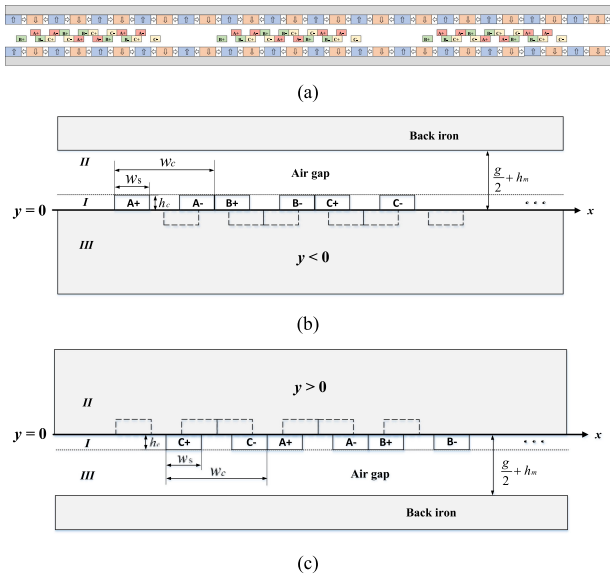

Fig. 4. Armature reaction subdomain model. (a) Proposed model. (b) Upper layer subdomain model. (c) Lower layer subdomain model.

finite length of moving primary [16]. It may reduce the accuracy of inductance calculation. Actually, the finite length of primary causes the nonperiodic distribution of current density, making it unable to be expanded into Fourier series. To solve this problem, it is assumed there are infinite groups of armature windings periodically distributed along the *x*-axis, which is called "virtual periodic primary." While the distance between adjacent armature windings τ_s is large enough, so that the coupling between adjacent windings is negligible with such a long distance. Under such condition, the current density distribution of each phase can be expressed by Fourier series.

As for asymmetric "virtual periodic primary" shown in Fig. 4(a), the upper layer has less coils than lower layer. So, the winding region should be divided into upper layer region and lower layer region. The overall armature reaction field is the superposition of magnetic fields generated by these two regions. Considering that the PMs are not excited, the upper layer and lower layer analytical model are both divided into three subregions: winding region; upper air-gap region; and lower air-gap region, as shown in Fig. 4(b) and (c).

The Maxwell equation of each region is as follows:

$$\begin{aligned} \nabla^2 \overrightarrow{A_I} &= -\mu_0 \overrightarrow{J_{A,B,C}} \\ \nabla^2 \overrightarrow{A_{II,III}} &= 0. \end{aligned} \tag{12}$$

As the armature windings are periodically distributed, the current density distribution $J(x)$ of phase A, B, C in the winding region can be expanded to Fourier series as follows:

$$\begin{cases} J_A(x) = \sum_{n=1}^{\infty} b_{na} \sin(k_n x) \\ J_B(x) = \sum_{n=1}^{\infty} b_{nb} \sin[k_n (x - w_c)] \\ J_C(x) = \sum_{n=1}^{\infty} b_{nc} \sin[k_n (x - 2w_c)] \end{cases} \tag{13}$$

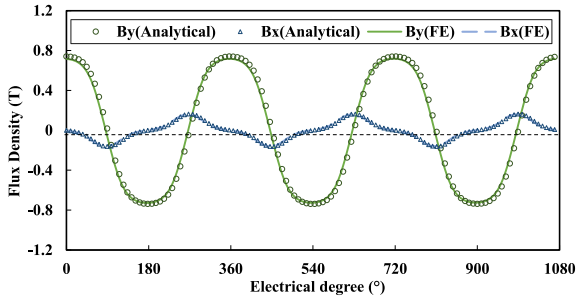

Fig. 5. Comparison of no-load PM field in the air-gap ($y = 1$ mm).

where the Fourier coefficient b_{ni} is given by (14) and $k_n = 2n\pi/\tau_s$

$$\begin{aligned} b_{ni} = & -\frac{2J_i}{n\pi}\left\{\cos\left[k_n\left(\frac{w_c}{2}\right)\right] - \cos\left[k_n\left(\frac{w_C}{2} - w_s\right)\right]\right\} \\ & i = a, b, c. \end{aligned} \tag{14}$$

The symmetric three-phase current densities J_i are given by

$$\begin{cases} J_a = N_s\, I_m \sin(wt) / (w_s h_c) \\ J_b = N_s\, I_m \sin(wt - 2\pi/3) / (w_s h_c) \\ J_c = N_s\, I_m \sin(wt - 4\pi/3) / (w_s h_c) \end{cases} \tag{15}$$

where I_m is the peak value of phase current and *w* is the angular frequency, respectively.

The boundary conditions for upper layer and lower layer subdomain model are given as

$$\begin{cases} {B_{yI}}'|_{y=h_c} = {B_{yII}}'|_{y=h_c};\ {H_{xI}}'|_{y=h_c} = {H_{xII}}'|_{y=h_c} \\ {B_{yI}}'|_{y=0} = {B_{yIII}}'|_{y=0};\ {H_{xI}}'|_{y=0} = {H_{xIII}}'|_{y=0} \\ {H_{xII}}'|_{y=\frac{g}{2}+h_m} = 0;\ {H_{xIII}}'|_{y=-\frac{g}{2}-h_m} = 0 \end{cases} \tag{16}$$

$$\begin{cases} {B_{yI}}'|_{y=-h_c} = {B_{yIII}}'|_{y=-h_c};\ {H_{xI}}'|_{y=-h_c} = {H_{xIII}}'|_{y=-h_c} \\ {B_{yI}}'|_{y=0} = {B_{yII}}'|_{y=0};\ {H_{xI}}'|_{y=0} = {H_{xII}}'|_{y=0} \\ {H_{xII}}'|_{y=\frac{g}{2}+h_m} = 0;\ {H_{xIII}}'|_{y=-\frac{g}{2}-h_m} = 0. \end{cases} \tag{17}$$

Hence, the armature reaction field solutions of each layer can be deduced by applying the boundary conditions above.

A. Calculation Results

Based on the former analytical model, the magnetic field is calculated, where the validation is conducted by 2-D FE model. Figs. 5 and 6 show the comparison of the air-gap flux density distributions between analytical model and FE model. It is illustrated that the results obtained by analytical model agree well with FE results.

For no-load PM field, the error mainly arises from the finite length of secondary. But, its influence can be omitted from Fig. 5. For armature reaction field, the error is big when using the analytical model with infinite length, i.e., applying the assumption (4). When considering the finite length of primary, the error mainly arises from the value of τ_s. In this article, $20\tau_p$ is enough to obtain an accurate result, as shown in Fig. 6.

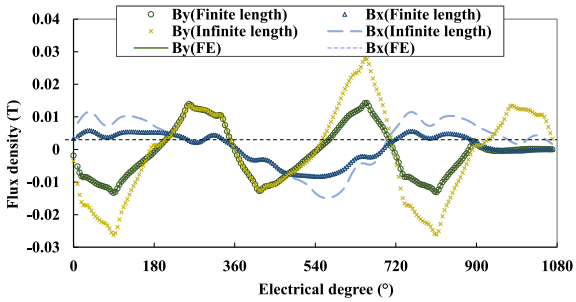

Fig. 6. Comparisons of armature reaction field in the air-gap ($y = 1$ mm) at $t = 0.003$ s (period $= 0.02$ s).

TABLE III
HARMONICS OF NO-LOAD AIR-GAP FLUX DENSITY

Model Type	Harmonic order		
	1st (T)	*3rd* (T)	*5th* (T)
Analytical	0.816	0.083	0.005
FE	0.797	0.080	0.005

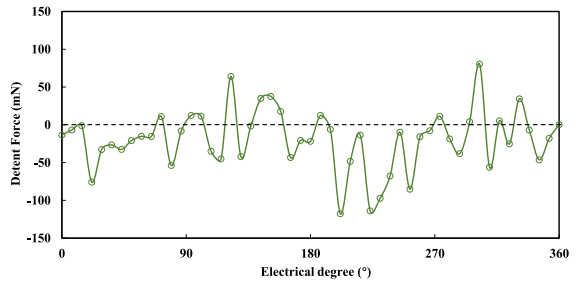

Fig. 7. Detent force of the DW-ILPMLSM.

Because the Halbach arrays are not ideal, results from analytical model and FE model both show that no-load air-gap flux density has some odd-order harmonics, as given in Table III.

IV. FORCE PERFORMANCE ANALYSIS

A. Force Characteristics

Usually, the thrust of a DM-ILPMLSM can be divided into two parts: detent force and electromagnetic thrust. As a result of ironless structure, the cogging force can be neglected. The detent force is mainly consist of end force and it can be simply obtained from no-load FE model, which is shown in Fig. 7. The air-gap length is 9.6mm and the maximum element length of air-gap is 0.5mm. From Fig. 7, the peak-to-peak value of detent force is 219 mN, only 0.31% of the average thrust obtained in the consequent analysis. Thus, the electromagnetic thrust is mainly analyzed in this article, regardless of the detent force.

For ILPMLSM, the electromagnetic thrust F_x can be easily computed by Lorentz's force law

$$F_x = \int (J \times B_{yI})\, dV \tag{18}$$

where B_{yI} is the normal component of the no-load air-gap flux density, J is the current density of armature winding, and V is the conductor volume. The total thrust exerted on a couple of coils $F_{x\mathrm{coil}}$ can be obtained by adding the thrust of upper layer coil to that of lower layer coil

$$F_{x\mathrm{coil}} = F_{x\mathrm{up}A} + F_{x\mathrm{low}A}. \tag{19}$$

The calculations of $F_{x\mathrm{up}A}$ and $F_{x\mathrm{low}A}$ are as follows:

$$\begin{aligned} F_{x\mathrm{up}A} &= \int_0^{h_c} \int_{-\frac{w_C}{2}+x_0}^{-\frac{w_C}{2}+w_s+x_0} J_a L B_{yI}\, dx dy \\ &\quad - \int_0^{h_c} \int_{\frac{w_C}{2}-w_s+x_0}^{\frac{w_C}{2}+x_0} J_a L B_{yI}\, dx dy \\ &= \sum_{n=1}^{\infty} A_F \sin h\,(m_n h_c) \end{aligned} \tag{20}$$

$$\begin{aligned} F_{x\mathrm{low}A} &= \int_{-h_c}^{0} \int_{-\frac{w_C}{2}+x_0+2\tau_p}^{-\frac{w_C}{2}+w_s+x_0+2\tau_p} J_a L B_{yI}\, dx dy \\ &\quad - \int_{-h_c}^{0} \int_{\frac{w_C}{2}-w_s+x_0+2\tau_p}^{\frac{w_C}{2}+x_0+2\tau_p} J_a L B_{yI}\, dx dy \\ &= \sum_{n=1}^{\infty} A_F \sin h\,(m_n h_c) \end{aligned} \tag{21}$$

where the coefficient A_F is given by

$$\begin{aligned} A_F = \frac{-2 J_a L B_{nI} \sin(m_n x_0)}{m_n} &\left\{ \cos\left[m_n \left(\frac{w_C}{2} - w_s \right) \right] \right. \\ &\left. - \cos\left(\frac{m_n w_C}{2} \right) \right\}. \end{aligned} \tag{22}$$

As can be seen from (20) and (21) that the thrust of any upper layer coil or lower layer coil has the same value. Hence, the overall thrust of phase A can be expressed by

$$F_{xA} = N_c\ F_{x\mathrm{up}A} = N_c \sum_{n=1}^{\infty} A_F \sin h\,(m_n h_c). \tag{23}$$

Similarly, the method can be applied to phase B and C. The overall thrust of the motor F_x can be obtained by superposition of thrust produced by each phase, which is finally simplified as

$$F_x = F_0 + N_c \sum_{n=2}^{\infty} (A_F + B_F + C_F) \sin h\,(m_n h_c) \tag{24}$$

where the coefficient B_F and C_F are as follows:

$$\begin{aligned} B_F = \frac{-2 J_b L B_{nI} \sin[m_n(x_0 + w_c)]}{m_n} &\left\{ \cos\left[m_n \left(\frac{w_C}{2} - w_s \right) \right] \right. \\ &\left. - \cos\left(\frac{m_n w_C}{2} \right) \right\} \end{aligned} \tag{25}$$

$$\begin{aligned} C_F = \frac{-2 J_c L B_{nI} \sin[m_n(x_0 + 2w_c)]}{m_n} &\left\{ \cos\left[m_n \left(\frac{w_C}{2} - w_s \right) \right] \right. \\ &\left. - \cos\left(\frac{m_n w_C}{2} \right) \right\}. \end{aligned} \tag{26}$$

The average thrust F_0 is given by

$$F_0 = -\frac{3N_cN_sI_mLB_{nI(n=1)}\sin h\left(m_nh_c\right)}{w_sh_cm_{n(n=1)}} \times \left\{\cos\left[m_n\left(\frac{w_C}{2}-w_s\right)\right]-\cos\left(\frac{m_nw_C}{2}\right)\right\}. \quad (27)$$

In conclusion, when the DW-ILPMLSM is fed by symmetrical three-phase current source, the average thrust can be calculated by (27). As can be seen from the second term in (24), the harmonics of no-load air-gap flux density will eventually lead to thrust ripple. But, the amplitude of these harmonics is small given in Table III, so the thrust ripple is tolerable in some high-precision applications.

Similarly, the normal force F_y can be obtained by the same way

$$F_y = \int (J \times B_{xI})\, dV. \quad (28)$$

Substituting the tangential component of the no-load air-gap flux density B_{xI} into (28), the normal forces of upper coil and lower coil are obtained as

$$\begin{cases} F_{y\mathrm{up}A} = \sum_{n=1}^{\infty} A_N\left[\cos h\left(m_nh_c\right)-1\right] \\ F_{y\mathrm{low}A} = \sum_{n=1}^{\infty} A_N\left[1-\cos h\left(m_nh_c\right)\right] \end{cases} \quad (29)$$

where the coefficient A_N is given by

$$A_N = \frac{2J_aLB_{nI}\cos\left(m_nx_0\right)}{m_n} \times \left\{\cos\left[m_n\left(\frac{w_C}{2}-w_s\right)\right]-\cos\left(\frac{m_nw_C}{2}\right)\right\}. \quad (30)$$

From (29), total normal force of a couple of coils is zero. Hence, if the number of upper layer coils and lower layer coils are equal (i.e., the total number of coils is even), the overall normal force can be eliminated. Although the structure of the 9s/6p DW-ILPMLSM is bilateral, it still has normal force as a result of nine coils in total. Besides, the normal force is proportional to current density *J*. So the impact of normal force in high electric loading can be significant.

B. Asymmetric Characteristics

The asymmetric windings may result in asymmetric electromagnetic parameters. The characteristics of inductances are studied firstly. Neglecting the effect of saturation, the inductances are independent of current. Besides, as the air-gap length is constant, the inductances are independent of position. Thus, the self- and mutual inductances can be obtained by flux linkage method shown as

$$L_{ij} = \frac{\psi_{ij}}{I_j} \quad (31)$$

where I_j is the current of excited phase, and ψ_{ij} is the flux linkage of another phase which is created by current I_j only. The expression of ψ_{ij} is given by

$$\psi_{ij} = N_c\, N_s \int B_{yI}{}' \cdot ds \quad (32)$$

TABLE IV
SELF AND MUTUAL INDUCTANCES

Inductance	L_a	L_b	L_c	M_{ab}= M_{ba}	M_{bc}= M_{cb}	M_{ac}= M_{ca}
Analytical (μH)	390.6	390.6	390.6	39.6	1.5	39.6
FE (μH)	385.3	384.4	386.1	39.4	0.5	39.7

where $B_{yI}{}'$ is the normal component of armature reaction flux density in the air-gap.

For example, when calculating the inductance of phase A, the flux linkage of upper layer is as follows:

$$\psi_{A\_\mathrm{up}} = \int_0^{h_c}\int_{\frac{w_C}{2}-w_S+x_0}^{\frac{w_C}{2}+x_0}\int_{-x_1}^{x_1}\rho_cL \times \left(B_{yI(0<y<h_c)up}+B_{yI(y>0)\mathrm{down}}\right)dxdx_1dy. \quad (33)$$

Similarly, the flux linkage of the phase A of lower layer is

$$\psi_{A\_\mathrm{low}} = \int_0^{h_c}\int_{\frac{w_C}{2}-w_S+x_0}^{\frac{w_C}{2}+x_0}\int_{-x_1}^{x_1}\rho_cL \times \left(B_{yI(0<y<h_c)\mathrm{up}}+B_{yI(y>0)\mathrm{down}}\right)dxdx_1dy \quad (34)$$

where $B_{yI(0<y<h_c)\mathrm{up}}$, $B_{yI(y<0)\mathrm{up}}$ is the flux density caused by upper layer windings of phase A, and $B_{yI(y>0)\mathrm{down}}$, $B_{yI(-h_c<y<0)\mathrm{down}}$ is caused by lower layer windings of phase A, and $\rho_c = N_s\,/(h_cw_s)$.

Adding the flux linkages of coils of upper and lower layers, the total flux linkages of phase *A* ψ_{AA} is obtained. Then, the self-inductance of the phase *A* is deduced by

$$L_a = \frac{\psi_{AA}}{I_A}. \quad (35)$$

When the phase *A* is excited, the total flux linkage of phase *B* can be computed by the same way. The mutual inductance is deduced by

$$M_{ba} = \frac{\psi_{BA}}{I_A}. \quad (36)$$

Table IV shows that the mutual inductance M_{bc} is far less than M_{ab} and M_{ac}, which demonstrates the asymmetry of mutual-inductances arise from the asymmetric double-layer winding rather than longitudinal end effect. However, the self-inductances still remain symmetric.

Generally, it is common to use current source in analysis. However, if the terminal currents are balanced, the force performance would not be affected by longitudinal end effect and the asymmetry of windings. Considering the real control situation, voltage source is recommended as the excitation to explore the asymmetric characteristics of DW-ILPMLSM.

When the motor is fed by a 29.6 V balanced voltage source, the waveform of resultant three-phase currents and the corresponding harmonics are shown in Fig. 8 and Table V, respectively. The current density in this case is about 5.8 A/mm^2. Because star-connection is applied in winding configuration, the third-harmonic is eliminated. The amplitude of seventh-harmonic is almost zero. The fundamental component is obviously asymmetric. So, the FE results proves that the resultant three-phase

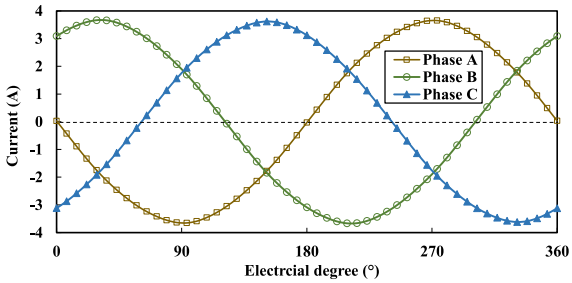

Fig. 8. Waveform of three-phase currents of the DW-ILPMLSM.

TABLE V
CURRENT HARMONICS

Harmonic order	I_A (A)	I_B (A)	I_C (A)
1st (50 Hz)	3.618	3.646	3.591
5th (250 Hz)	0.026	0.028	0.028
7th (350 Hz)	0.004	0.008	0.007

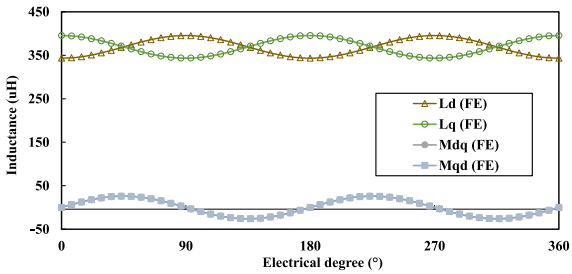

Fig. 9. *D*- and *q*-axis inductances of the DW-ILPMLSM.

currents are unbalanced. As the three-phase voltage source applied is balanced, the main cause is the asymmetric inductances.

As a result, the asymmetry of inductances may lead to the increase of thrust ripple. To explore the origin of thrust ripple, the three-phase inductances, PM flux linkages and three-phase currents are transformed *dq* reference frame through the Park transformation. As can be seen from Table IV, the three-phase self-inductances have the same value denoted as L_1. Assuming that $M_{ab} = M_{ac} = M_1$, $M_{bc} = M_2$, the differences between mutual inductances $\Delta M = M_1 - M_2$. Hence, the three-phase inductance matrix $[L_{ss}]$ is given by

$$[L_{ss}] = \begin{bmatrix} L_1 & M_1 & M_1 \\ M_1 & L_1 & M_2 \\ M_1 & M_2 & L_1 \end{bmatrix}. \tag{37}$$

The *d*- and *q*-axis inductance matrix $[L_{dq}]$ is shown in (38), the relationship between $[\mathrm{L_{ss}}]$ and $[\mathrm{L_{dq}}]$ is given by (39). Because the inductances are asymmetric, the *d*- and *q*-axis mutual-inductances M_{dq}, $M_{qd} \neq 0$. Besides, the *d*- and *q*-axis inductances L_d and L_q alternate at a double fundamental frequency. The FE results of *d*- and *q*-axis inductances shown in Fig. 9 also confirm it

$$[L_{dq}] = \begin{bmatrix} L_d & M_{dq} \\ M_{qd} & L_q \end{bmatrix} \tag{38}$$

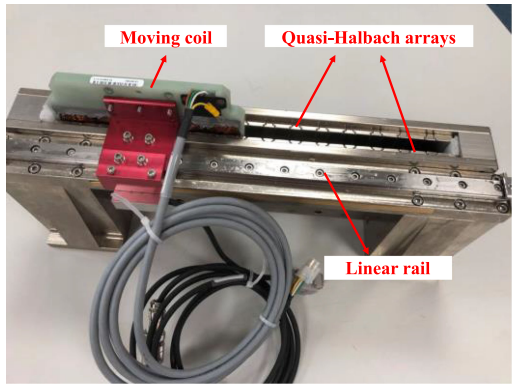

Fig. 10. Prototype of the DW-ILPMLSM.

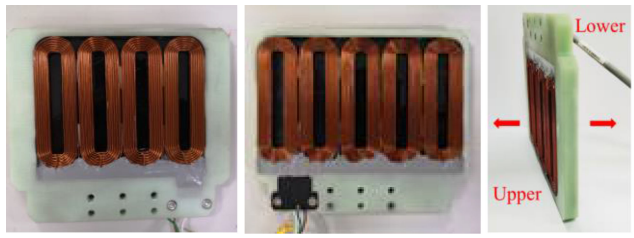

Fig. 11. Primary structure of the DW-ILPMLSM. (a) Upper layer coils. (b) Lower layer coils. (c) Mover.

$$\begin{cases} L_d = \left(L_1 - M_2 - \frac{2}{3}\Delta M\right) - \frac{2}{3}\Delta M \cos 2\theta \\ L_q = \left(L_1 - M_2 - \frac{2}{3}\Delta M\right) + \frac{2}{3}\Delta M \cos 2\theta \\ M_{dq} = M_{qd} = \frac{2}{3}\Delta M \sin 2\theta. \end{cases} \tag{39}$$

The *d*- and *q*-axis flux linkages ψ_d , ψ_q are given by

$$\begin{cases} \psi_{\mathrm{d}} = L_d\, I_d + M_{dq} I_q + \psi_{\mathrm{f}} \\ \psi_{\mathrm{q}} = M_{dq}\, I_d + L_q I_q \end{cases} \tag{40}$$

where ψ_{f} is the PM flux linkage. If $I_d = 0$ control strategy is applied in practical application and assume other conditions are ideal, the overall thrust is thus given by

$$F = \frac{3\pi}{2\tau_p}\left[\frac{2}{3}\Delta M I_q^2 \sin 2\theta + \psi_{\mathrm{f}} I_q\right]. \tag{41}$$

As a result, the thrust will fluctate at a doubly fundamental frequency arising from asymmetric inductance parameters. However, ΔM is about 38.1 uH in this case. Thus, the thrust ripple is less than 0.1% of the average thrust.

V. PROTOTYPE AND EXPERIMENT

To verify the proposed analytical model, a 9s/6p DW-ILPMLSM has been prototyped, as shown in Fig. 10. Detail of primary structure is shown in Fig. 11, including coils of the upper [see Fig. 11(a)] and lower layer [see Fig. 11(b)]. Two layers windings are tightly glued on the epoxy resin, and then two parts are fixed together as mover [see Fig. 11(c)]. The specification of the prototype is the same as those given in Table I.

The test platform is shown in Fig. 12. The experimental measurement of back-EMF is carried out first and compared

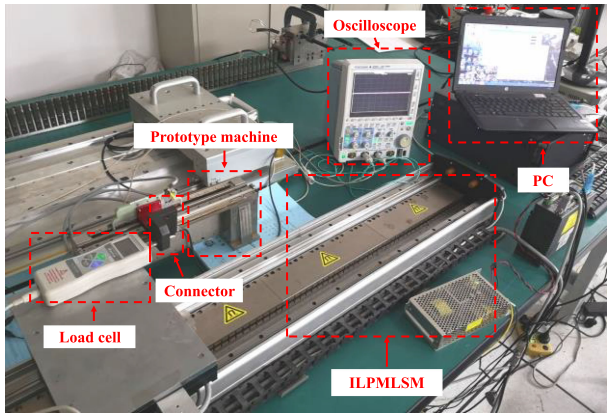

Fig. 12. Test platform of the DW-ILPMLSM.

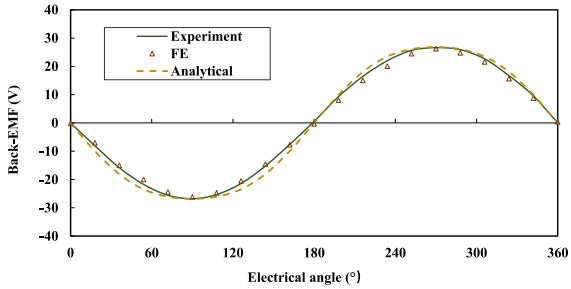

Fig. 13. Comparison of predicted and measured back-EMFs of the prototyped DW-ILPMLSM.

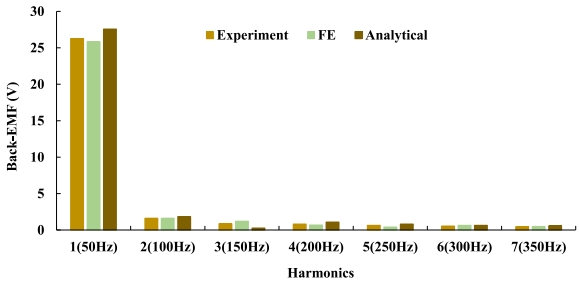

Fig. 14. FFT results of predicted and measured back-EMFs of the prototyped DW-IPMLSM.

with analytical and FE results. The prototype motor is driven by another ILPMLSM with a constant speed of 60 mm/s.

Fig. 13 compares the back-EMFs (phase A) obtained by analytical model, FE model and experimental test, and the Fast Fourier Transform (FFT) results of back-EMFs are given in Fig. 14. It shows that the analytical prediction of back-EMF is in good agreement with FE and experimental results. The amplitude error between calculated back-EMF and experimental result may arise from the magnetic flux leakage, end windings and mechanical tolerances.

Fig. 15 gives the thrusts obtained by the analytical model, FE model and experimental test under the unit current of 1 A. One load cell with full scale of 500 N and precision of 0.2% is used to measure the thrust. The difference is mainly due to measurement errors of the load cell under the small detent force condition. The

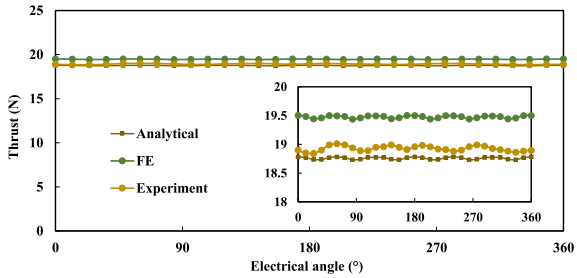

Fig. 15. Comparison of predicted and measured thrusts of the prototype DW-ILPMLSM with the mover position.

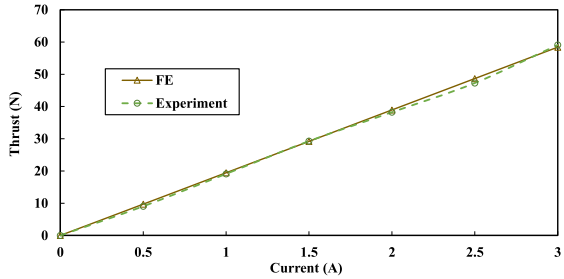

Fig. 16. Comparison of predicted and measured thrusts of the prototype DW-ILPMLSM with the increase of the peak current.

total computational time of proposed analytical model is only 0.0194s, compared with the 38min16s of the FE method (CPU is Intel i5-8250U, and RAM is 8 GB). Besides, the variation of the thrust with peak current is statically measured, as shown in Fig. 16. The thrust is basically linear with the amplitude of peak current, and the analytical results agree well with the experiment results.

VI. Conclusion

In this article, an accurate analytical model considering finite length of moving primary is established. As the finite length of primary causes the nonperiodic distribution of current density, "virtual periodic primary" is introduced as infinite groups of armature windings periodically distributed along the x-axis. Because the two winding layers are asymmetrical, the magnetic field of each layer should be computed independently. As a result, the analytical solutions of characteristics in terms of back-EMF, thrust, normal force, self- and mutual inductances have been derived. The analytical model saves a lot of time compared with the FE method, thus it is helpful for optimizing the motor. And the results match well with corresponding experiments.

After investigating the influences of asymmetric structure analytically and numerically, it is found when DW-ILPMLSM is fed by symmetric current source, the force ripple mainly comes from harmonics of no-load field. When DW-ILPMLSM is fed by symmetric voltage source, the asymmetric inductances caused by asymmetric double-layer windings, together with the resultant unbalanced currents lead to the increase of force ripple. When appropriate control method is applied, the force ripple can be small enough for precise applications.

REFERENCES

[1] N. Fujii and K. Okinaga, "X-Y linear synchronous motors without force ripple and core loss for precision two-dimensional drives," *IEEE Trans. Magn.*, vol. 38, no. 5, pp. 3273–3275, Sep. 2002.

[2] D. L. Trumper, W. -J. Kim, and M. E. Williams, "Design and analysis framework for linear permanent-magnet machines," *IEEE Trans. Ind. Appl.*, vol. 32, no. 2, pp. 371–379, Mar./Apr. 1996.

[3] S. -M. Jang and S. -H. Lee, "Comparison of two types of PM linear synchronous servo and miniature motor with air-cored film coil," *IEEE Trans. Magn.*, vol. 38, no. 5, pp. 3264–3266, Sep. 2002.

[4] G. Zhou, X. Huang, H. Jiang, L. Tan, and J. Dong, "Analysis method to a halbach PM ironless linear motor with trapezoid windings," *IEEE Trans. Magn.*, vol. 47, no. 10, pp. 4167–4170, Oct. 2011.

[5] B. Xia, J. X. Shen, P. C. Luk, and W. Z. Fei, "Comparative study of air-cored axial-flux permanent-magnet machines with different stator winding configurations," *IEEE Trans. Ind. Electron.*, vol. 62, no. 2, pp. 846–856, Feb. 2015.

[6] W. Mei, Q. Lu, and Q. Jiang, "Comparative analysis of an air-core PMLSM with new double-layer windings," in *Proc. IEEE Int. Magn. Conf.*, Apr. 23-27, 2018, pp. 1–5.

[7] Z. Xie, J. Zhang, W. Mei, and Q. Lu, "Investigation of a novel ironless linear synchronous machine with Double-layer winding and quasi-halbach magnets," in *Proc. Int. Conf. Elect. Mach. Syst.*, Aug. 11–14, 2019, pp. 1–6.

[8] J. W. Jansen, J. P. C. Smeets, T. T. Overboom, J. M. M. Rovers, and E. A. Lomonova, "Overview of analytical models for the design of linear and planar motors," *IEEE Trans. Magn.*, vol. 50, no. 11, Nov. 2014, Art. no. 8206207.

[9] G. Akoun and J.-P. Yonnet, "3D analytical calculation of the forces exerted between two cuboidal magnets," *IEEE Trans. Magn.*, vol. 20, no. 5, pp. 1962–1964, Sep. 1984.

[10] L. Li, Y. Tang, B. Kou, and M. Ma, "Design and analysis of ironless linear electromagnetic launcher with high thrust density for space platform," in *Proc. 16th Int. Symp. Electromagn. Launch Technol.*, May 15–19, 2012, pp. 1–6.

[11] A. H. Isfahani, "Analytical framework for thrust enhancement in permanent-magnet (PM) linear synchronous motors with segmented PM poles," *IEEE Trans. Magn.*, vol. 46, no. 4, pp. 1116–1122, Apr. 2010.

[12] Y. Zhang, Z. Yang, M. Yu, K. Lu, Y. Ye, and X. Liu, "Analysis and design of double-sided air core linear servo motor with trapezoidal permanent magnets," *IEEE Trans. Magn.*, vol. 47, no. 10, pp. 3236–3239, Oct. 2011.

[13] A. Rahideh, A. Ghaffari, A. Barzegar, and A. Mahmoudi, "Analytical model of slotless brushless PM linear motors considering different magnetization patterns," *IEEE Trans. Energy Convers.*, vol. 33, no. 4, pp. 1797–1804, Dec. 2018.

[14] L. Zhang, B. Kou, F. Xing, and B. Zhao, "Characteristic analysis of an ironless linear synchronous motor with novel halbach magnet array," in *Proc. 17th Int. Symp. Electromagn. Launch Technol.*, Jul. 2014, pp. 1–5.

[15] Q. Lu, B. Wu, Y. Yao, Y. Shen, and Q. Jiang, "Analytical model of permanent magnet linear synchronous machines considering end effect and slotting effect," *IEEE Trans. Energy Convers.*, vol. 35, no. 1, pp. 139–148, Mar. 2020.

[16] M. Ma, L. Li, Z. He, and C. C. Chan, "Influence of longitudinal end-effects on electromagnetic performance of a permanent magnet slotless linear launcher," *IEEE Trans. Plasma Sci.*, vol. 41, no. 5, pp. 1161–1166, May 2013.

[17] K. Shin, H. Cho, S. Lee, and J. Choi, "Armature reaction field and inductance calculations for a permanent magnet linear synchronous machine based on subdomain model," *IEEE Trans. Magn.*, vol. 53, no. 6, Jun. 2017, Art. no. 8105804.

[18] L. Yan, L. Zhang, Z. Jiao, H. Hu, C. Chen, and I. Chen, "Armature reaction field and inductance of coreless moving-coil tubular linear machine," *IEEE Trans. Ind. Electron.*, vol. 61, no. 12, pp. 6956–6965, Dec. 2014.

[19] S. Ouagued, Y. Amara, and G. Barakat, "Cogging force analysis of linear permanent magnet machines using a hybrid analytical model," *IEEE Trans. Magn.*, vol. 52, no. 7, Jul. 2016, Art. no. 8202704.

[20] E. Kazan and A. Onat, "Modeling of air core permanent-magnet linear motors with a simplified nonlinear magnetic analysis," *IEEE Trans. Magn.*, vol. 47, no. 6, pp. 1753–1762, Jun. 2011.

[21] Z. Q. Zhu, D. Ishak, D. Howe, and J. Chen, "Unbalanced magnetic forces in permanent-magnet brushless machines with diametrically asymmetric phase windings," *IEEE Trans. Ind. Appl.*, vol. 43, no. 6, pp. 1544–1553, Nov./Dec. 2007.

[22] Z. Q. Zhu, M. L. Mohd Jamil, and L. J. Wu, "Influence of slot and pole number combinations on unbalanced magnetic force in PM machines with diametrically asymmetric windings," *IEEE Trans. Ind. Appl.*, vol. 49, no. 1, pp. 19–30, Jan./Feb. 2013.

[23] G. -H. Kang, J. -P. Hong, and G. -T. Kim, "Permanent-magnet linear brushless motor by using equivalent magnetizing current," *IEEE Trans. Ind. Appl.*, vol. 37, no. 5, pp. 1241–1247, Sep./Oct. 2001.

Zhedong Xie was born in Ningbo, China, in 1996. He received the B.Eng. in electrical engineering, in 2018 from Zhejiang University, Hangzhou, China, where he is currently working toward the M.Sc. degree at the College of Electrical Engineering.

His research interests include analysis and control of permanent magnet linear machines.

Qinfen Lu (Senior Member, IEEE) received the B.Eng., M.Sc., and Ph.D. degrees from Zhejiang University, Hangzhou, China, in 1996, 1999, and 2005, respectively, all in electrical engineering.

Since 1999, she has been with the College of Electrical Engineering, Zhejiang University, where she is currently a Professor. Her research interests include analysis and control of linear machines, permanent-magnet machines, etc.

Weihu Mei was born in Tiantai, China, in 1994. He received the M.Sc. in electrical engineering from Zhejiang University, Hangzhou, China, in 2019.

His research interests include analysis and control of permanent magnet linear machines.

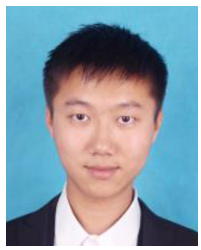

Yanxin Li received the B.Eng. and M.Eng. degrees in electrical engineering from Zhejiang University, Hangzhou, China, in 2011 and 2014, respectively, and the Ph.D. degree from the University of Sheffield, Sheffield, U.K., in 2018.

Since 2020, he has been a as a Tenure-tracked Associate Professor with the Zhejiang University. His major research interests include the modeling, design, and analysis of linear machine.